ic mechanism it is not known whether the differences in the matrix elements corresponding to hopping on $(^{13}C_{0.5}{}^{12}C_{0.5})_{60}$ versus $^{13}C_{60}$ and $^{12}C_{60}$ clusters will give rise to significant variations in T_c, or whether these differences are averaged in the mean-field model used to estimate T_c. Calculations for the electronic model are needed to address this essential issue.

Our experimental isotope effect data obtained on a series of specifically substituted Rb_3C_{60} superconductors provide an unambiguous value for the isotope shift in completely substituted fullerene superconductors and elucidate a unique difference between intermolecular and intramolecular isotopic substitution. A theoretical understanding of these experimental results may lead to a single viable mechanism for superconductivity in the fullerenes.

REFERENCES AND NOTES

1. A. F. Hebard *et al.*, *Nature* **350**, 660 (1991).
2. M. J. Rosseinsky *et al.*, *Phys. Rev. Lett.* **66**, 2830 (1991).
3. K. Holczer *et al.*, *Science* **252**, 1154 (1991).
4. C.-C. Chen, S. P. Kelty, C. M. Lieber, *ibid.* **253**, 886 (1991).
5. K. Tanigaki *et al.*, *Nature* **352**, 222 (1991).
6. C. M. Varma, J. Zaanen, K. Raghavachari, *Science* **254**, 989 (1991).
7. M. Schluter, M. Lannoo, M. Needels, G. A. Baraff, D. Tomanek, *Phys. Rev. Lett.* **68**, 526 (1992).
8. I. I. Mazin *et al.*, *Phys. Rev. B* **45**, 5114 (1992).
9. D. L. Novikov, V. A. Gubanov, A. J. Freeman, *Physica C* **191**, 399 (1992).
10. S. Chakravarty, M. P. Gelfand, S. Kivelson, *Science* **254**, 970 (1991).
11. G. Baskaran and E. Tossatti, *Curr. Sci.* **61**, 33 (1991).
12. J. Bardeen, L. N. Cooper, J. R. Schrieffer, *Phys. Rev.* **108**, 1175 (1957).
13. P. Morel and P. W. Anderson, *ibid.* **125**, 1263 (1962).
14. W. L. McMillan, *ibid.* **167**, 331 (1968).
15. A. P. Ramirez *et al.*, *Phys. Rev. Lett.* **68**, 1058 (1992).
16. T. W. Ebbesen *et al.*, *Nature* **355**, 620 (1992).
17. A. A. Zakhidov *et al.*, *Phys. Lett. A* **164**, 355 (1992).
18. S. Chakravarty, S. A. Kivelson, M. I. Salkola, S. Tewari, *Science* **256**, 1306 (1992).
19. C.-C. Chen and C. M. Lieber, *J. Am. Chem. Soc.* **114**, 3141 (1992).
20. Y. Chai *et al.*, *J. Phys. Chem.* **95**, 7564 (1991).
21. F. Diederich *et al.*, *Science* **252**, 548 (1991).
22. We prepared materials with similar grain sizes by using identical procedures to isolate the isotopically substituted C_{60} solids from solution and to dope these solids with Rb.
23. It is also possible to define T_c as the point of maximum curvature in the magnetization data (*15*). Analysis of our data using this definition yields isotope shifts that are similar to the values reported in the text.

24. We acknowledge helpful discussions with P. Allen, M. Tinkham, and E. Kaxiras. We thank E. Mazur and J.-K. Wang for helpful advice during the initial stages of the laser ablation experiments, and A. N. Tyler for the mass spectroscopy measurements. C.M.L. acknowledges partial support of this work by the David and Lucile Packard Foundation. The mass and nuclear magnetic resonance spectroscopy facilities are supported by grants from NIH and NSF.

11 September 1992; accepted 25 November 1992

Element-Specific Magnetic Microscopy with Circularly Polarized X-rays

J. Stöhr, Y. Wu, B. D. Hermsmeier, M. G. Samant, G. R. Harp, S. Koranda, D. Dunham, B. P. Tonner

Circularly polarized soft x-rays have been used with an imaging photoelectron microscope to record images of magnetic domains at a spatial resolution of 1 micrometer. The magnetic contrast, which can be remarkably large, arises from the fact that the x-ray absorption cross section at inner-shell absorption edges of aligned magnetic atoms depends on the relative orientation of the photon spin and the local magnetization direction. The technique is element-specific, and, because of the long mean free paths of the x-rays and secondary electrons, it can record images of buried magnetic layers.

Polarized light has long been used to probe the magnetic properties of matter in the visible spectral range. Two prominent methods for examining the magnetic properties of solids are based on observing changes in light polarization upon reflection, the magneto-optical Kerr effect, or upon transmission, the Faraday effect (*1*). Because the energy of visible light is a few electron volts, the Kerr and Faraday effects involve electronic transitions from the valence to the conduction band. In the late 1980s, Schütz and co-workers demonstrated (*2*) that circularly polarized x-rays may also be used as a probe of magnetism. In the so-called magnetic circular x-ray dichroism (MCXD) technique, the difference in absorption between right and left circularly polarized x-rays is measured at an inner-shell absorption edge in magnetic materials. The uniqueness of the technique lies in the elemental specificity afforded by tuning to the characteristic atomic absorption edges. For transition metals, MCXD measurements typically involve p to d core-to-valence excitations near L_3 or L_2 edges (*2–4*).

We describe here the use of the MCXD technique for magnetic imaging. We have recorded pictures of magnetic bits on a CoPtCr magnetic recording disk with a lateral resolution of 1 μm obtained by use of circularly polarized soft x-rays with energies near the Co L_3 (778 eV) and L_2 (793 eV) edges and by detection and imaging of the secondary electrons from the sample with a photoemission microscope (*5*). Our results show that the contrast is remarkably large, such that images can be recorded without background subtraction. Our results were obtained on disks with protective overcoats of 130 Å of carbon and about 40 Å of an organic fluorocarbon lubricant, which emphasizes the power of the technique for technological applications. Besides being element-specific, MCXD microscopy has the advantage over conventional Kerr microscopy (*1*) that its diffraction-limited lateral resolution is tens rather than thousands of angstroms (*6*). We anticipate by straightforward extrapolation that it will be possible to achieve a lateral resolution of around 100 Å by 100 Å with state-of-the-art electron imaging systems (*7*) and enhanced x-ray intensities from insertion devices on electron storage rings (*8*).

The experiments were performed at the Stanford Synchrotron Radiation Laboratory (SSRL). X-ray absorption spectra with linearly polarized x-rays were recorded on the wiggler beamline 10-1, and the MCXD measurements were carried out on the bending magnet beamline 8-2, both of which are equipped with spherical grating monochromators. We obtained circularly polarized x-rays by moving an aperture and the prefocusing mirror below the plane of the electron orbit, yielding a degree of circular polarization of $(I^R - I^L)/(I^R + I^L) = 90 \pm 5\%$, where I^R and I^L are the x-ray intensities with right and left circular polarization, respectively. For the MCXD spectra two pieces cut from the same sample were remanently magnetized parallel to the surface but in opposite directions. Spectra were recorded at a grazing x-ray incidence angle of 20° with the photon spin of the right circularly polarized x-rays aligned either parallel or antiparallel to the magnetization direction of the two samples, respectively.

In the MCXD microscopy experiments we used an ultrahigh-vacuum–compatible photoelectron microscope based on secondary electron yield detection (width of kinetic energy distribution about 6 eV) (*5*). The device has a two-stage electrostatic lens system with a contrast aperture in the back-focal plane of the objective lens. The magnified image of the sample (adjustable field

J. Stöhr, Y. Wu, M. G. Samant, G. R. Harp, Almaden Research Center, IBM Research Division, 650 Harry Road, San Jose, CA 95120.
B. D. Hermsmeier, IBM San Jose, 5600 Cottle Road, San Jose, CA 95153.
S. Koranda, D. Dunham, B. P. Tonner, Synchrotron Radiation Center, University of Wisconsin–Madison, Stoughton, WI 53589.

of view up to 500 μm in diameter) is amplified by a double microchannel plate array and projected onto a phosphor screen. The image on the screen is monitored with a video camera outside the vacuum. The camera output is then digitized by a frame grabber, which can integrate the image signal and store images digitally. The image is captured at video rates with the computer integrating the captured images at a rate of about ten frames per second. In our experiments, the x-rays were incident at an angle of 30° from the surface and the secondary electrons were accelerated into the microscope along the surface normal.

The x-ray absorption spectrum of the disk sample, recorded by total electron yield detection (9), is shown in the upper curve in Fig. 1A. It reveals the K-shell absorption edges of the carbon overcoat, the oxygen and fluorine constituents of the polymer overcoat, and the L edges of the Cr and Co atoms in the CoPtCr magnetic material. The Co L edge is seen even though the magnetic material is covered by 130 Å of carbon and about 40 Å of the fluorocarbon polymer. The bottom curve in Fig. 1A was recorded after the sample had been exposed for 5 min to broad-band synchrotron radiation ("zero order light," see below). Polarization-dependent x-ray absorption spectra recorded at the Co L edges with magnetization and photon spin parallel and antiparallel to each other, and their difference curve, the dichroism spectrum, are shown in Fig. 1, B and C, respectively. The spectra shown are normalized to the incident photon flux and rescaled to a constant step height far above the Co L edges. The dichroism effect is quite large at the L_3 and L_2 resonance positions, and its sign is opposite at the two edges (3, 4). It is this difference that provides a means of obtaining contrast in a magnetic microscopy experiment.

In order to exploit the dichroism effect for microscopy, we used a magnetic recording disk, identical to that used for Fig. 1, and wrote a repeating test pattern on it at various recording densities. The pattern consisted of magnetic domains (bits) with alternating in-plane magnetization directions and rows of different size bits of dimensions 10 μm by 10 μm, 10 μm by 2 μm, 10 μm by 1 μm, and 10 μm by 0.5 μm. Images were recorded at three different photon energies: 770 eV, below the Co L edges; 778 eV, at the Co L_3 resonance energy; and 793 eV, at the Co L_2 resonance energy. In photoelectron microscopy, which is based on the detection of secondary electrons, image contrast arises from differences in the number of secondary electrons created in different microscopic areas of the sample. In MCXD microscopy, the photon energy is tuned to an absorption edge resonance where the absorption cross section

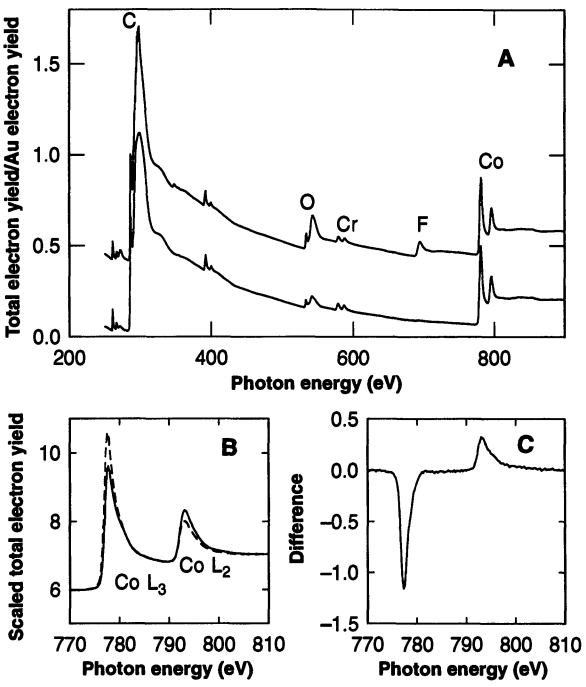

Fig. 1. (**A**) X-ray absorption spectra, recorded by total electron yield detection with linearly polarized x-rays, of a CoPtCr magnetic recording disk covered with 130 Å of carbon and about 40 Å of a fluorocarbon polymer (top curve) and after 5 min of exposure to "zero order light" (bottom curve). We have separated the curves by shifting the top curve up by 0.1 unit and the bottom curve down by 0.2 unit. Unmarked small peaks in the curves are due to higher order x-ray radiation. (**B**) X-ray absorption spectra near the Co L edges of the same sample recorded at a grazing x-ray incidence angle of 20° with circularly polarized x-rays and parallel (dashed line) and antiparallel (solid line) alignment of photon spin and magnetization vectors, respectively. The data were scaled to the same jump far above the edge. (**C**) Dichroism spectrum obtained by taking the difference between the spectra in (B).

exhibits a large dichroism effect as seen in Fig. 1, B and C. Because the secondary electron yield from the sample is proportional to the x-ray absorption cross section (9), it changes locally as a function of the relative alignment of photon spin and magnetization direction, revealing the element-specific magnetic domain structure.

Before recording images of magnetic domains, we viewed the surface in real time using "zero order light" for alignment purposes and inspection of the surface topography. Analysis of the disk sample after this procedure revealed a loss of fluorine in the thin polymer overcoat, as shown in Fig. 1A. MCXD images recorded at different photon energies and a field of view of 200 μm are shown in Fig. 2A. The images required an integration time of about 5 min. The Co L- edge MCXD spectra (Fig. 2B) illustrate the correspondence between images and photon energies. At a photon energy below the L edges, the image looks rather homogeneous, indicating that no magnetic contrast exists. Two light spots arise from topological inhomogeneities, perhaps dust particles, and faint lines attributable to substrate texture can also be recognized. The image taken at the Co L_3 resonance energy reveals an alternating black and white pattern of squares and, in the row below, rectangles of the same height but narrower width. At the Co L_2 resonance energy the same pattern is observed but with reversed contrast. This is due to the inversion of the dichroism effect as seen in the MCXD spectra in Fig. 2B. The observed pattern is that of the written magnetic bits, the squares having a dimension of 10 μm by 10 μm and the bits in the second row measuring 10 μm by 2 μm. The rows of the smaller sized bits below are only visible as lines without internal contrast.

Images of the bit patterns taken at higher magnification exhibited statistically limited contrast across the field of view owing to low signal intensity. In this case we obtained an image with enhanced contrast by simply subtracting the scaled images taken at the Co L_3 and L_2 energies. The resulting image is shown in Fig. 3A. Now, even the bits in the third row, which have dimensions 10 μm by 1 μm, are resolved. The bit images in Fig. 3A, especially the bottom two rows, show a curvature that is not an artifact of the imaging optics. Rather, it results from a curvature in the write-pole pieces in the read-write head as confirmed by direct investigation of the head. In Fig. 3B we have plotted the relative image intensity as a function of distance along the three rows of bits, respectively. The plotted "average pixel value" corresponds to the intensity integrated over most of the vertical size of the bits. The contrast for the bottom row of bits (10 μm by 1 μm) is decreased to about one-third that of the top row (10 μm by 10 μm) as a result of resolution limitations. Our resolution limit is close to 1 μm.

The resolution limit in our experiment is set by aberrations of the electrostatic lenses. An uncorrected astigmatism is present because of machining errors, and a large chromatic aberration blurs the image because of the relatively large energy width of the secondary electron distribution. These specific problems can be overcome by the

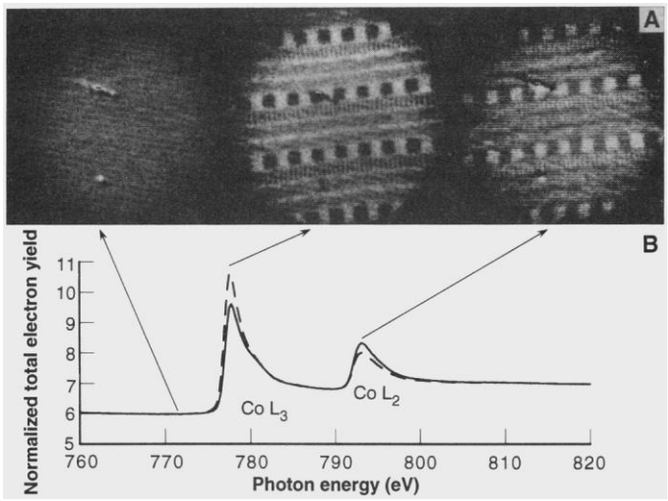

Fig. 2. (**A**) MCXD images of magnetic domains on a magnetic recording disk, recorded with right circularly polarized x-rays of different energies, as indicated. We obtained the images shown by dividing the original images by a corresponding image taken at a photon energy of 810 eV to remove the nonuniform response of the optical system across the field of view. The disk was similar to that used for Fig. 1, with rows of magnetic domains of dimensions 10 μm by 10 μm, 10 μm by 2 μm, 10 μm by 1 μm, and 10 μm by 0.5 μm, respectively. The magnetization direction of the domains lies along the rows but alternately points to the right and left in the figure. The x-rays were incident at an angle of 30° from the surface, along the horizontal axis of the figure, that is, at a slight azimuthal angle relative to the rows of bits. (**B**) The Co L-edge dichroism spectra, which correlate photon energies and images.

inclusion of a stigmatic optical element and an electron energy filter (*10*). The useful magnification is limited in part by the available photon flux density, as discussed in more detail below.

In addition to using circularly polarized x-rays and a photoelectron microscope for magnetic microscopy, other procedures based on x-rays can be designed. One approach would be to focus circularly polarized x-rays into the smallest possible spot and scan the sample while monitoring the electron or fluorescence yield. In the soft x-ray region, spot sizes of a few hundred angstroms have been achieved (*11*). Fluorescence yield detection (*9*) would allow one to probe layers that are buried under thousands (depending on the photon energy) of angstroms of material. The disadvantage of the x-ray microprobe approach is that the spatial resolution is degraded at grazing x-ray incidence angles, which are needed to probe samples with in-plane magnetic domain structure, because the spot size is geometrically enlarged.

It is clear that the acquisition time and lateral resolution will be dramatically improved as brighter synchrotron radiation sources and improved electron or photon imaging systems become available. Let us estimate the practical resolution limit of the present imaging approach. It has been demonstrated that electron imaging systems are capable of a spatial resolution of about 100 Å by 100 Å (*7*). The question is whether a sufficient photon flux density can be generated to obtain a measurable signal in a reasonable time (a few minutes) from such a small area. For the present experiment the monochromator was operated with wide-open slits (400 μm), and, at a storage ring current of 50 mA, we had a flux of about 2×10^{11} photons per second in a spot size of 0.5 mm^2. Because this flux density is sufficient to image domains of size 1 μm^2, we thus require an increase in flux density of 10^4. This increase is indeed possible with undulator insertion devices (*8*) (factor of 100 in flux) and suitable x-ray focusing optics (*11*) (factor of 100 in spot size). In addition, the flux increases linearly with storage ring current, and currents ten times higher are possible. For scanning MCXD microscopy similar estimates can be made. In this case, focal spot sizes near 100 Å require the coherent illumination of an x-ray optic and hence the brightness of the source is the figure of merit (*11*). Again, enhancement factors of 10^4 to 10^5 will become available with the advent of third-generation synchroton radiation sources (*12*). In the future we therefore predict a practical spatial resolution limit of MCXD microscopy near 100 Å by 100 Å.

Finally, we address the question whether MCXD microscopy has any significant merits or even unique capabilities relative to other magnetic imaging techniques, such as Bitter microscopy (*13*), Kerr microscopy (*14*), Lorentz microscopy (*15*), scanning electron microscopy with polarization analysis (SEMPA) (*16*), spin-polarized low-energy electron microscopy (SPLEEM) (*17*), or magnetic force microscopy (MFM) (*18*). Three unique capabilities of MCXD microscopy stand out: elemental specificity, "chemical state" specificity, and variable probing depth. As discussed earlier, the elemental specificity comes from the ability to tune the x-ray energy to the characteristic atomic absorption edges. The "chemical state" specificity of MCXD arises from the fact that the near-edge x-ray absorption fine structure (NEXAFS) (*9*) is sensitive to the charge state and the local bonding and coordination of a given element. Thus, if an element is present in the sample in more than one "chemical state," it is possible in many cases to correlate the different states with specific peaks in the NEXAFS spectrum. The dichroism effect of these peaks would then be characteristic of the magnetic properties of the element in the particular "chemical state" (*4*). In this context, another unique aspect of using x-rays is that one can obtain magnetic, chemical, and even structural information on the same microscopic area by combining MCXD with NEXAFS and extended x-ray absorption fine structure (EXAFS) measurements, the latter two being typically carried out with linearly polarized radiation. One can change the probing depth of MCXD microscopy by using different detection modes to measure electron yields (*9*), or, in the future, fluorescence yield detection in conjunction with scanning. By use of Auger electron or partial electron yield detection, it will be possible to image magnetic domains of thin overlayers on surfaces, down to monolayer thickness; secondary electron yield or fluorescence yield detection allows the investigation of buried layers.

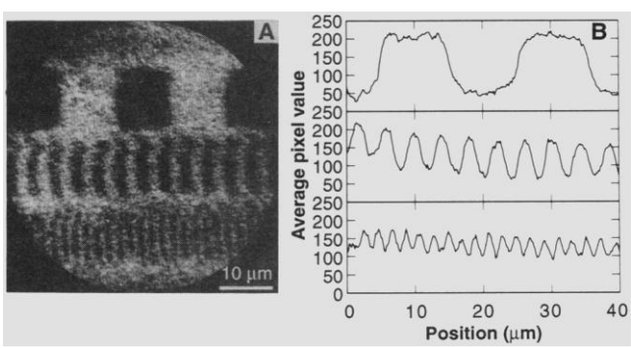

Fig. 3. (**A**) High-resolution MCXD images obtained by subtracting images obtained at the L_3 and L_2 edges for enhanced contrast and by removing a slight intensity slope in the vertical direction caused by a small misalignment of the sample normal relative to the optical axis of the electron lens. (**B**) Image intensity averaged over most of the vertical bit height plotted as a function of the distance along the rows.

REFERENCES AND NOTES

1. D. E. Fowler, in *Encyclopedia of Materials Characterization*, C. R. Brundle, C. A. Evans, Jr., S. Wilson, Eds. (Butterworth-Heinemann, Boston, 1992), pp. 723–735.
2. G. Schütz *et al.*, *Phys. Rev. Lett.* **58**, 737 (1987); G. Schütz *et al.*, *Z. Phys. B* **73**, 67 (1988); G. Schütz *et al.*, *ibid.* **75**, 495 (1989).
3. C. T. Chen, F. Sette, Y. Ma, S. Modesti, *Phys. Rev. B* **42**, 7262 (1990).
4. F. Sette, C. T. Chen, Y. Ma, S. Modesti, N. V. Smith, in *X-Ray Absorption Fine Structure*, S. S. Hasnain, Ed. (Ellis Horwood, Chichester, United Kingdom, 1991), pp. 96–105.
5. B. P. Tonner and G. R. Harp, *Rev. Sci. Instrum.* **59**, 853 (1988); ———, S. F. Koranda, J. Zhang, *ibid.* **63**, 564 (1992).
6. The diffraction limit can be overcome by near-field optical techniques, as discussed by: D. W. Pohl, in *Advances in Optical and Electron Microscopy*, C. J. R. Sheppard and T. Mulvey, Eds. (Academic Press, London, 1990), pp. 243–312; E. Betzig and J. K. Trautman, *Science* **257**, 189 (1992).
7. E. Bauer, in *Chemistry and Physics of Solid Surfaces VIII*, R. Vanselow and R. Howe, Eds. (Springer, Berlin, 1990), pp. 264–287; R. M. Tromp and M. C. Reuter, *Ultramicroscopy* **36**, 99 (1991).
8. K. J. Kim, *SPIE* **1345**, 116 (1990).
9. J. Stöhr, *NEXAFS Spectroscopy* (Springer Series in Surface Sciences 25, Springer, Heidelberg, 1992).
10. B. P. Tonner, *Nucl. Instrum. Methods Phys. Res. A* **291**, 60 (1990).
11. For a review, see *X-Ray Microscopy II*, D. Sayre, M. Howells, J. Kirz, H. Rarback, Eds. (Springer Series in Optical Sciences 56, Springer, Heidelberg, 1988); J. Voss *et al.*, *J. X-ray Sci. Technol.* **3**, 85 (1992).
12. Advanced Light Source Handbook (PUB-643 Rev. 2, Lawrence Berkeley Laboratory, University of California, April 1989) (unpublished).
13. B. D. Cullity, *Introduction to Magnetic Materials* (Addison-Wesley, Reading, MA, 1972), chap. 9; M. Hartmann, *J. Magn. Magn. Mater.* **68**, 298 (1987).
14. W. Rave, R. Schäfer, A. Hubert, *J. Magn. Magn. Mater.* **65**, 7 (1987).
15. J. N. Chapman, *J. Phys. D.* **17**, 623 (1984).
16. M. R. Scheinfein, J. Unguris, M. H. Kelley, D. T. Pierce, R. J. Celotta, *Rev. Sci. Instrum.* **61**, 2501 (1990).
17. M. S. Altman *et al.*, *Mater. Res. Soc. Symp. Proc.* **232**, 125 (1991).
18. D. Rugar *et al.*, *J. Appl. Phys.* **68**, 1169 (1990).

19. We are grateful to G. Castro for initiating the photoelectron microscopy effort at IBM Almaden; S. Lambert for writing the bit pattern on the disk; and D. Pierce, H. Poppa, R. Browning, and I. McFadyen for helpful discussions. The work was carried out in part at SSRL, which is operated by the Department of Energy, Division of Chemical Sciences.

23 September 1992; accepted 25 November 1992

Reaction of a Tantalum Alkylidene Complex with Dinuclear Metal Carbonyls: Formation of C_3 Ligands

Grant Proulx and Robert G. Bergman*

The mechanisms of reactions that deoxygenate carbon monoxide (CO) and convert it into longer chain hydrocarbons are not well understood. A series of reactions between "early" and "late" transition metal complexes that result in CO coupling reactions in a homogeneous solution are reported. In one example, the Schrock tantalum-methylene complex $(\eta^5\text{-}C_5H_5)_2Ta(CH_2)(CH_3)$ reacts with the dinuclear metal carbonyls $Co_2(CO)_8$ and $Fe_2(CO)_9$ in a novel fashion to yield a $C_3H_2O_2$ ligand bridging three metal centers. Reaction of the tantalum-methylene complex with $Re_2(CO)_{10}$ leads to an even more substantial change in which extensive rearrangement along with three-carbon coupling occurs. An oxygen atom is removed from one CO group, leading to the novel oxotantalum compound $(\eta^5\text{-}C_5H_5)_2(CH_3)Ta{=}O$. Simultaneously, the carbon atom from the transformed CO couples with two CH_2 groups initially bound to tantalum and the CH_2 hydrogens are rearranged to produce a CH_3–CC ligand. Low-temperature nuclear magnetic resonance and isotope tracer experiments have provided preliminary information about the mechanisms of these unusual carbon-carbon bond-forming reactions.

Carbon monoxide (CO) is an important potential building block in chemical synthesis (*1*). "Synthesis gas," a mixture of CO and H_2, is used in metal surface-catalyzed chemical transformations, such as the Fischer-Tropsch process, that lead to longer chain organic molecules. These reactions have been studied by ultrahigh vacuum (UHV) techniques, and surface-bound carbide, CH, and CH_2 fragments have been implicated as intermediates (*1*, *2*). However, their mechanisms are still not well understood. A few analogous homogeneous solution reactions are known in which CO molecules are coupled (*3–6*) or cleaved (*7*, *8*), but more extensive homogeneous C–C bond-forming processes with this ligand are still rare. Examples of CO oligomerization processes that occur in a homogeneous solution would provide an opportunity for detailed study of this fundamental transformation.

We report the reaction between the first "early" (left side of the periodic table) transition metal (alkyl) (methylene) complex, prepared by Schrock in 1975 (*9*), and three "late" (right side) dinuclear metal carbonyls: $Co_2(CO)_8$, $Fe_2(CO)_9$, and $Re_2(CO)_{10}$. In spite of the superficial similarity of the carbonyls, the reaction proceeds similarly in two of these cases but takes a dramatically different course in the third. With Co and Fe, two CO ligands and a CH_2 fragment directly couple with one another. In the Re system, a number of substantial changes take place: hydrogens are rearranged in two CH_2 groups to give a carbon atom and a methyl group; an oxygen atom is removed from a CO ligand and transferred to a second tantalum moiety [generating the novel complex $Cp_2(CH_3)Ta{=}O$ ($Cp = \eta^5\text{-}C_5H_5$)]; and the resulting carbon fragments are coupled to give a coordinated C_3 (methylacetylide) ligand.

Treatment of 1 eq (equivalent) of $Cp_2Ta(CH_2)(CH_3)$ (**1**) with 1 eq of $Co_2(CO)_8$ or $Fe_2(CO)_9$ above −30°C for 3 hours resulted in >90% [^{1}H nuclear magnetic resonance (NMR)] yields of dark brown and dark red compounds, respectively, with the stoichiometries $Cp_2Ta(CH_3)(C_3H_2O_2)Co_2(CO)_6$ (**2**) and $Cp_2Ta(CH_3)(C_3H_2O_2)Fe_2(CO)_7$ (**3**). Compound **2** was isolated in 49% yield and compound **3** in 47% yield by benzene-pentane recrystallization. The ^{1}H NMR spectra (*10*, *11*) of **2** and **3** are similar, with two doublets attributable to two coupled inequivalent CH_2 protons. The ^{13}C NMR spectra (*10*, *11*) of **2** and **3** are also quite similar with resonances attributable to an allylic CH_2 and a Ta–CH_3 ligand. The spectroscopic data eliminate structures for these compounds that retain the CH_2 ligand on the Ta center and suggest attack of this group on a CO ligand.

To confirm this inference, the x-ray structures of **2** and **3** were determined. The molecular geometries are shown in Fig. 1, A and B. These show heterotrinuclear structures in which a $(C_3H_2O_2)$ unit, formed from the direct coupling of two CO ligands and the carbene C atom, bridges the three metal centers and is bound to the Ta through two O atoms. One late metal center is associated in an allylic fashion with all three carbons of the ligand, and the second late metal center is bound to only a single C atom of this ligand (*12*, *13*).

In contrast to the above results, treatment of 2 eq of **1** with 1 eq of the larger 5*d* metal carbonyl $Re_2(CO)_{10}$ for 1 hour above 5°C resulted in the formation of a deep red compound in 62% isolated yield [based on $Re_2(CO)_{10}$] with the stoichiometry $Cp_2Ta(C_3H_3)Re_2(CO)_9$ (**4**). Overall, formation of **4** requires a net loss of H_2O from **1** and the metal carbonyl. However, free H_2O was not produced in this reaction; instead, $Cp_2Ta(O)(CH_3)$ (**5**) (*14*, *15*) and CH_4 were formed. Control experiments demonstrated that treatment of **1** with

Department of Chemistry, University of California, Berkeley, CA 94720.

*To whom correspondence should be addressed.